Observation of Multi-Directional Energy Transfer in a Hybrid Plasmonic–Excitonic Nanostructure

Tommaso Pincelli,* Thomas Vasileiadis, Shuo Dong, Samuel Beaulieu, Maciej Dendzik, Daniela Zahn, Sang-Eun Lee, Hélène Seiler, Yingpeng Qi, R. Patrick Xian, Julian Maklar, Emerson Coy, Niclas S. Mueller, Yu Okamura, Stephanie Reich, Martin Wolf, Laurenz Rettig, and Ralph Ernstorfer*

Hybrid plasmonic devices involve a nanostructured metal supporting localized surface plasmons to amplify light–matter interaction, and a non-plasmonic material to functionalize charge excitations. Application-relevant epitaxial heterostructures, however, give rise to ballistic ultrafast dynamics that challenge the conventional semiclassical understanding of unidirectional nanometal-to-substrate energy transfer. Epitaxial Au nanoislands are studied on WSe_2 with time- and angle-resolved photoemission spectroscopy and femtosecond electron diffraction: this combination of techniques resolves material, energy, and momentum of charge-carriers and phonons excited in the heterostructure. A strong non-linear plasmon–exciton interaction that transfers the energy of sub-bandgap photons very efficiently to the semiconductor is observed, leaving the metal cold until non-radiative exciton recombination heats the nanoparticles on hundreds of femtoseconds timescales. The results resolve a multi-directional energy exchange on timescales shorter than the electronic thermalization of the nanometal. Electron–phonon coupling and diffusive charge-transfer determine the subsequent energy flow. This complex dynamics opens perspectives for optoelectronic and photocatalytic applications, while providing a constraining experimental testbed for state-of-the-art modelling.

1. Introduction

Irradiation of nanometals with light drives collective oscillations of charge-carriers (plasmons) and light localization beyond the diffraction limit in plasmonic near-fields. The energy of plasmons dissipates within tens of femtoseconds, either radiatively by photon emission, or in electron–hole excitations, producing non-equilibrium carrier distributions.

In recent years, the focus of plasmonics is oriented toward plasmonic energy harvesting.[1–3] The nascent field of hybrid plasmonics seeks to interface metal nanostructures with other materials, and in particular semiconductors, which convert plasmons to electronic excitations with impactful applications. Hybrid plasmonics devices are useful in light-harvesting, photochemistry, photocatalysis, photodetectors, and single-molecule detectors.[2,4–7] For these applications, radiative losses are

T. Pincelli, T. Vasileiadis, S. Dong, S. Beaulieu, M. Dendzik, D. Zahn, S.-E. Lee, H. Seiler, Y. Qi, R. P. Xian, J. Maklar, M. Wolf, L. Rettig, R. Ernstorfer
Fritz-Haber-Institut der Max-Planck-Gesellschaft
Faradayweg 4-6, 14195 Berlin, Germany
E-mail: pincelli@fhi-berlin.mpg.de
T. Pincelli, R. Ernstorfer
Institut für Optik und Atomare Physik
Technische Universität Berlin
Straße des 17. Juni 135, 10623 Berlin, Germany
E-mail: ernstorfer@tu-berlin.de
T. Vasileiadis
Faculty of Physics
Adam Mickiewicz University
Uniwersytetu Poznanskiego 2, Poznan 61-614, Poland

S. Beaulieu
Université de Bordeaux - CNRS - CEA
CELIA, UMR5107, Talence F33405, France
M. Dendzik
Department of Applied Physics
KTH Royal Institute of Technology
Hannes Alfvéns väg 12, Stockholm 114 19, Sweden
H. Seiler, N. S. Mueller, Y. Okamura, S. Reich
Freie Universität Berlin
Arnimallee 14, 14195 Berlin, Germany
Y. Qi
Center for Ultrafast Science and Technology
School of Physics and Astronomy
Shanghai Jiao Tong University
Shanghai 200240, China
R. P. Xian
Department of Statistical Sciences
University of Toronto
700 University Avenue, Toronto M5G 1Z5, Canada
E. Coy
NanoBioMedical Centre
Adam Mickiewicz University
ul. Wszechnicy Piastowskiej 3, Poznań PL 61614, Poland

suppressed, e.g., by minimizing the metallic nanoparticles' volume,[8] while hot-carrier injection is maximized by creating a strong exciton–plasmon interaction. This is achieved when the plasmonic hot carriers ejection is more efficient than internal thermalization by electron–phonon coupling.

The challenges in the microscopic description of hybrid plasmonic systems stem from the strong inhomogeneity of the hot-carrier distributions both in real space and, for the case of crystals with well-defined Bloch states, also in reciprocal space. In these conditions, the assumptions of homogeneous hot carrier generation and instant thermalization (that proved effective for larger nanoparticles in colloidal suspensions) are no longer applicable: geometry-assisted intraband transitions dominate plasmon decoherence dynamics enhancing the hot carrier distribution at the surface,[9,10] narrow gaps between the nanoparticles generate regions of enhanced polarization of the substrate,[11] and unoccupied states in the semiconductor offer high-energy excitation transitions across the interface at selected momentum matched locations.[12,13] Furthermore, the coupling of the electronic system with phononic excitations, and the subsequent energy flow leading back to thermodynamic equilibrium, are critical in determining the subsequent functionalities achievable by devices based on the hybrid interface.[14]

We focus on achieving a fundamental understanding of how electron-plasmon interaction influences the interfacial energy flow in a rapidly emerging class of heterostructures formed by noble metals interfaced with transition metal dichalcogenides (TMDs). The 2D van der Waals crystals, with their long lived and strongly bound excitons, promise a unique playground for hybrid plasmonics, and have been proven to exhibit strong exciton–plasmon coupling up to room temperature.[15,16] The TMD–noble metal interface has been realized both in configurations where the TMD has a nanoscale structure[17–19] and in devices where the 3D metal is laterally confined.[15,16,20–23] Nano-TMDs on extended Au present fascinating possibilities for the control of surface plasmons owing to their large dielectric functions[18] and have enjoyed a significant effort devoted to understanding the microscopic mechanisms behind interfacial dynamics and band alignment.[17,19,24,25] We focus, instead, on nano-structured Au on extended TMD, which has been recently employed to realize several devices with advanced plasmonic functionality[20,23] or strong coupling,[15,16,21,22] but whose investigation of microscopic mechanisms has been less extensive.

Satisfactory modeling of microscopic charge-transfer mechanisms has been recently achieved with ab initio calculations that go beyond the simple jellium model,[13,26] but disentangling the same processes experimentally is challenging, as it requires monitoring several microscopic subsystems and their couplings at femtosecond timescales, as shown in **Figure 1**a. The vast majority of experimental studies employed time-resolved optical spectroscopies,[21,22] with techniques that have

limited access to optically dark excitations and to the details of quasiparticle scattering pathways in momentum space. We propose an approach that offers the opportunity to ground the study of plasmonic dynamics with an unprecedented detail of physical evidence, resolving the dynamics of the electronic states in momentum space and the coupling of charge excitations to phonons: this provides a direct response to the needs of hybrid plasmonics as foreseen by Linic et al.[3]

Here, we study a heterostructure of Au nanoislands on WSe_2 (Figure 1a) with angle-resolved photoemission spectroscopy (ARPES) and time-resolved ARPES (tr-ARPES) that give access to equilibrium and excited electronic states with momentum resolution[17,27,28] (Figure 1b), capture excitons in the TMD[29] and detect the dynamic hot-carrier distributions in the nano-metal.[30] To fully unfold the dynamics of the system we investigate also the complementary subsystem, the lattice, by femtosecond electron diffraction (FED)[31–33] (Figure 1c), determining the coupling of electronic excitations to phononic states.

Further support is provided by electronic structure calculations using density functional theory and finite elements calculations to investigate the distribution of interfacial fields. With this toolset, we show that strong exciton–plasmon interactions can produce multi-directional charge- and energy-flow between metal and semiconductor at extremely short time-scales, a picture rather different from what is expected in traditional plasmonic approaches and semiclassical models both at the femtosecond and picosecond timescale. By determining the origins and timescales of such transient energy transfers, our results provide important insight for the design of a wide set of hybrid heterostructures that are object of very active investigation,[34–36] as well as an accurate and constraining experimental test for the advanced theoretical models being developed for hybrid plasmonics.

2. Results

The Au nanoislands grow epitaxially on bulk WSe_2 with a random distribution of sizes and shapes, as displayed by transmission electron microscopy (TEM) micrography in Figure 1d. The average lateral size and thickness are 10 and 2 nm, respectively (see Section S1, Supporting Information). Optical absorption spectroscopy of bare and Au-decorated WSe_2 shows a significant modification of the absorbance (Figure 1e): a suppression of the WSe_2 A-exciton peak is accompanied by an increased absorption at $\lambda \geq 800$ nm which, as we will show, arises from localized, plasmon-assisted photoabsorption in the nanoparticle array. The stochastic distribution of sizes and shapes results in a broadly varying enhancement of the absorption within the bandgap of the semiconductor, rather than peaked resonances.[37] In the following, we demonstrate that Au decoration tailors the pump electric field at the surface, producing a twofold effect: generation of localized surface plasmons (LSP) on the nanoislands, and strong field enhancement at the uncovered WSe_2 surface.

To gain insight on the optical response, we perform finite-element-method (FEM) calculations (see Experimental Section and Section S3, Supporting Information). We model the nanoparticles by vectorizing a part of the micrograph in Figure 1d,

N. S. Mueller
NanoPhotonics Centre
Cavendish Laboratory
Department of Physics
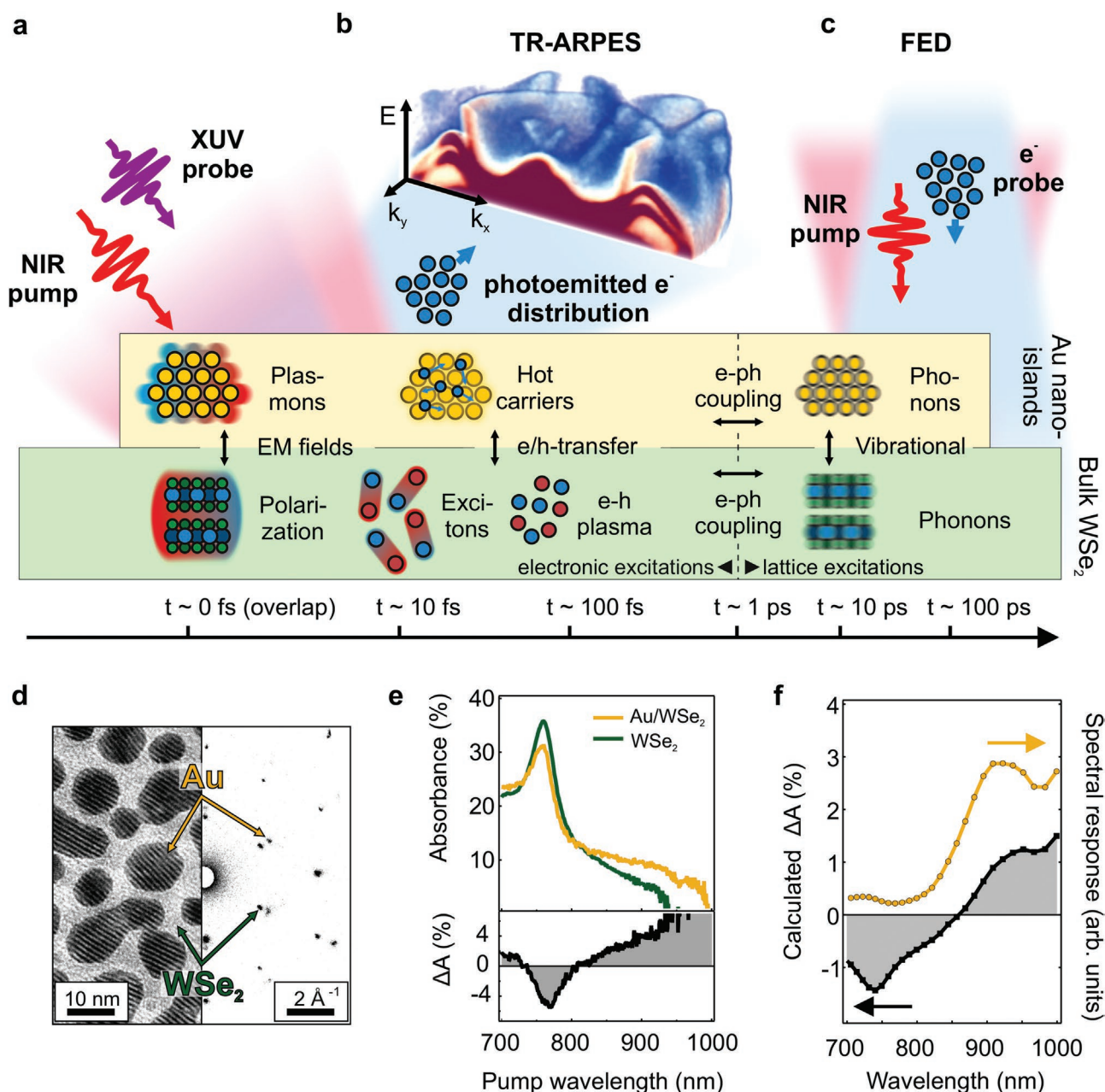University of Cambridge
JJ Thomson Avenue, Cambridge CB30HE, UK

Figure 1. Subsystem- and material-resolved study of ultrafast energy flow in a nanometal–semiconductor heterostructure. a) Schematic illustration of the techniques employed to probe different microscopic subsystems and their couplings in the heterostructure. Optical excitation by a pump pulse generates plasmons and hot carriers in the nanometal, and excitons in the semiconductor, probed by tr-ARPES (schematically represented in (b). In both materials the lattice degrees of freedom (phonons) are excited by electron–phonon coupling, probed by FED (schematically represented in (c) and the right part of (f). Interfacial interactions involve: electromagnetic fields (LSP and interfacial potentials), charge and energy transfer (Meitner–Auger, Föster or Dexter coupling) and vibrational coupling. b) Cut-out (for $k_y > 0$) of the 3D ARPES signal $I(k_x,k_y,E)$ from the heterostructure surface with 21.7 eV Extreme ultraviolet (XUV) excitation. In a tr-ARPES experiment, one of such volumetric datasets is acquired for each pump–probe delay. c) Scheme of a transmission FED experiment. d) Electron microscopy (left) and electron diffraction (right) of epitaxial Au nanoislands (dark in the microgscopy image) on single-crystalline multilayer flakes of WSe$_2$. In a FED experiment, performed in transmission geometry, one of such diffractograms is acquired for every pump–probe delay. e) Top: Light absorption spectra of pure (green line) and Au-decorated WSe$_2$ (yellow line). Bottom: Wavelength-dependent relative change of the absorption (ΔA) due to Au decoration. f) Black squares: Calculated relative change of absorption using finite difference modeling (see Experimental Section). Golden circles: spectral response of the electric field integral.

to reproduce a realistic arrangement of shapes. We obtain the far-field absorbance variation due to the presence of Au decoration, which broadly matches the spectral distribution of the

experimental result (black curves in Figure 1e,f). Discrepancies in amplitude and spectral distributions can be explained with the experimental uncertainty on the effective thickness

of the individual sample, combined with the use of reference optical spectra and the limited size of the calculation (see Experimental Section). The FEM calculations enable estimating the contribution of plasmon-induced hot-carriers to the increased absorbance (yellow circles in Figure 1f, see Experimental Section). The total absorbance variation (black curve) is adequately represented at photon energies smaller than the WSe$_2$ bandgap, thus confirming that, in this spectral range, photoabsorption in Au is dominated by plasmonic generation of injectable hot-carriers.[38–40] Since the nanoislands thickness is below the inelastic mean free path (IMFP) of hot carriers in Au[41] and the out-of-plane momentum matching constraints are relaxed due to strong vertical confinement, virtually all the plasmon-generated hot-carriers energetically above the Schottky barrier are available for injection.

For high peak power excitation, easily achieved with ultrashort light pulses, absorption also involves non-linear multiphoton processes. Close examination of the electric fields (see Section S2, Supporting Information) shows a strong field enhancement of up to 30 times in the semiconductor near the nanoislands edges, which can induce multiphoton absorption. The amplitude and depth penetration of the field enhancement in WSe$_2$ increase as the photon energy becomes smaller than the A-exciton energy. In this spectral range, WSe$_2$ becomes more transparent and the plasmonic fields propagate further below the surface. Therefore, at high optical excitation intensities and long (≥850 nm) wavelengths, we expect the photoabsorption in WSe$_2$ to occur predominantly by multiphoton processes.

From the volumetric ARPES data displayed in Figure 1b, we extract isoenergy maps of the momentum distribution. At the Fermi energy, the hexagonal sp-band and Shockley surface state form the Fermi surface of Au (111) (**Figure 2**a, top panel). At $E - E_F = -0.8$ eV (Figure 2a, bottom panel), we observe that the ARPES signal appears as the superposition of Au (111) and WSe$_2$ bandstructures, with the Au sp-band surrounded by the hexagonal arrangement of WSe$_2$ valence band maxima (VBM). By selecting a momentum direction ($\overline{\Gamma} - \overline{K}$ in the 2D Brillouin zone of WSe$_2$, black line in Figure 2a), we extract a momentum-energy map, and compare with ab initio calculations (see Section S3, Supporting Information) employing density functional theory (DFT) as overlaid on the data in Figure 2b. While the calculations have been performed for the two separate materials, the good agreement between DFT and experiment suggests a weak hybridization across the van der Waals gap (see Section S4, Supporting Information).

The ARPES data combined with further core-level photoemission experiments reveal the details of band alignment (Figure 2c): considering the Schottky–Mott theory of contact potential, the Fermi level would be expected to be energetically near the valence band maximum. However, owing to the work function reduction observed in Au nanoparticles[42] and interfacial dipoles formation, the Fermi level is closer to the conduction band minimum of WSe$_2$, with Schottky barrier $\Phi_e = 0.470 \pm 0.005$ eV for electrons and $\Phi_h = 1.000 \pm 0.005$ eV for holes[43] (see Section S5, Supporting Information). With this configuration, interfacial band bending is strongly suppressed, although a potential well of ≈170 meV still exists, in the proximity of the nanoparticle interface.

2.1. Electron Dynamics

To explore the charge dynamics during and right after the plasmonic excitation, we perform time-resolved ARPES experiments. Four observables, sketched in Figure 2d, allow us to distinguish the evolution of each material. In the semiconductor, we detect both the occupied band position and the photoexcited population in the conduction band. The time resolved experimental technique adds an additional dimension to the data and allows to capture transient population and scattering dynamics.[27,29] In Au, we can track the dynamical evolution of the chemical potential, i.e., the energy position of the Fermi distribution center, and the electronic temperature. The main features involved in the dynamics are contained in a single momentum-energy cut (gray squares in Figure 2a).

In bare WSe$_2$ at room temperature, 800 nm pumping excites resonantly the A-exciton,[29] thanks to the large bandwidth of 40 fs pulses. The excitons, observable as a transient population at the K-points (Figure 2e), scatter rapidly (18 ± 4 fs[27,29]) to momentum-indirect states, with electrons populating the conduction band minimum (Σ valley) and holes occupying local valence band maxima (K or Γ points). The lifetime of indirect excitons is long owing to the suppressed radiative recombination probability arising from momentum mismatch.[29,44,45] We observe a bi-exponential population decay, with the shortest lifetime of 1.5 ± 0.1 ps (see Section S6, Supporting Information) likely determined by hot exciton diffusion in the bulk and surface defect recombination.[46] In the heterostructure, 800 nm pumping at room temperature produces excited carriers in both Au and WSe$_2$ (Figure 2f, see also Figure S4, Supporting Information). To disentangle the contributions, we perform two measurements: one at room temperature, and another after cooling the heterostructure to 70 K (see also **Figure 3**e). The reduction of temperature in this system produces an increase of the WSe$_2$ bandgap (in optical measurements: ≈60 meV[47]), tuning the exciton resonance out of the pump bandwidth, which we will consider as the small detuning regime.

Figure 3a reports the electronic temperature (T_e) dynamics of Au obtained by fitting the data to Fermi–Dirac distributions (see Section S11, Supporting Information). Compared to the well-known electron–lattice equilibration dynamics of bulk Au (see Section S12, Supporting Information, shown in Figure 3a as a result of two-temperature model), the experimental T_e of the heterostructure rises on a longer timescale and to a lesser degree. This suggests efficient charge-transfer from the Au nanoislands to WSe$_2$, to such an extent that Au hot carriers are transferred before the non-equilibrium distribution can thermalize, a signature of strong exciton–plasmon interaction. The observation of plasmon-induced hot-carrier transfer is further supported by tracking the position of WSe$_2$ VBM and the chemical potential in the small detuning case (Figure 3b). The two features shift simultaneously in opposite directions, indicating that unbalanced amounts of charge are being transferred across the interface. These observations match optical measurements and FEM calculations, where we highlighted the relevance of LSP-induced injectable hot carriers in the absorption spectrum of the heterostructure (see Section S8 and S9, Supporting Information).
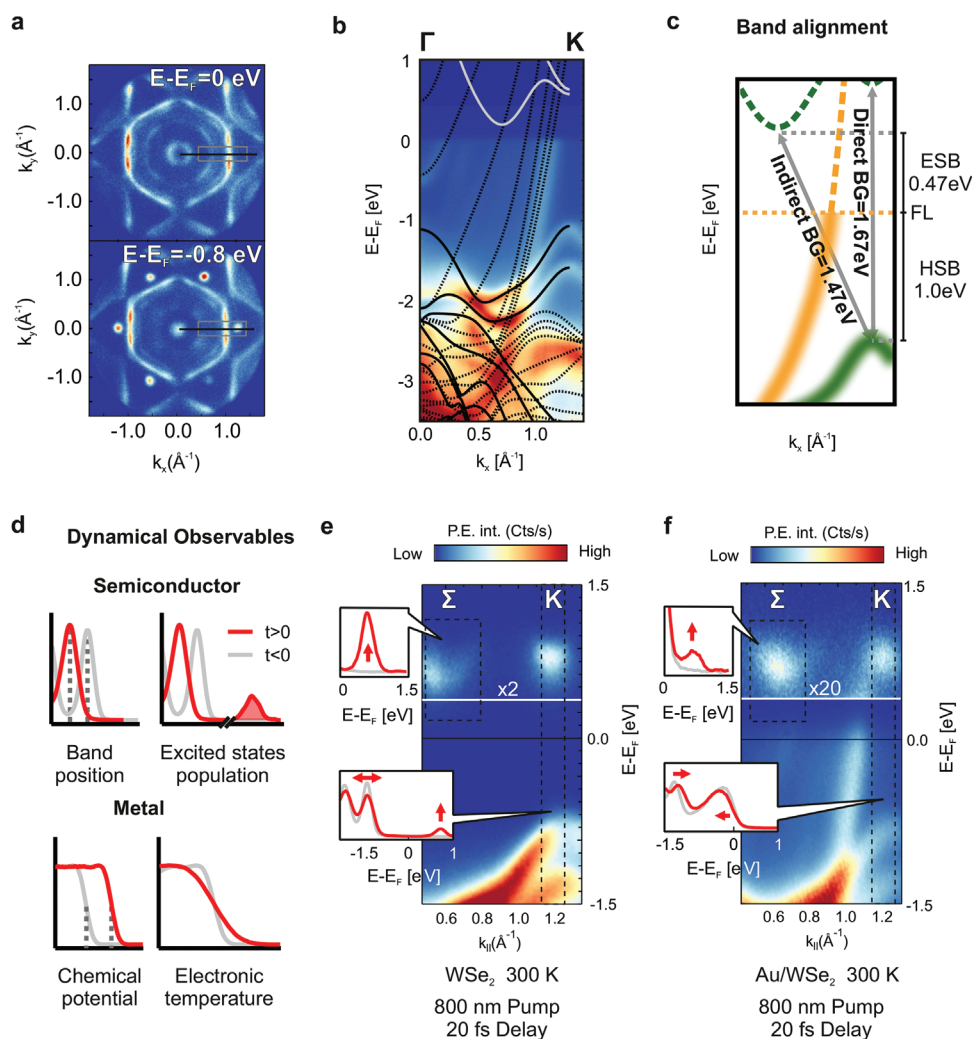
Figure 2. Electronic structure of Au/WSe$_2$. a) Constant energy cuts of Au/WSe$_2$ in the first Brillouin zone. Top: Fermi surface $E - E_F = 0$ eV, with hexagonal sp-band and surface state (close to the Γ point), characteristic of the Au(111) facet. Bottom panel: isoenergy surface at $E - E_F = -0.8$ eV, showing the VBM at the K-points of WSe$_2$ (hexagonal array of dots). The black line (gray rectangle) shows the energy–momentum cut probed in (b) ((f)). b) Γ–K momentum–energy cut of Au/WSe$_2$. The solid black and white curves show the valence and conduction bands of WSe$_2$ as derived by DFT. The dashed curves show the DFT-derived metallic states of Au. c) Schematic picture of the band alignment: at the WSe$_2$ K points, the direct bandgap (DBG) is 1.67 eV, larger than the indirect bandgap (IBG) at 1.47 eV. Due to nanostructuring, the Fermi Level (FL) position is closer to the conduction band than expected from the Schottky–Mott limit, with electron and hole Schottky barriers (ESB and HSB) of 0.47 and 1 eV, respectively. d) Schematic summarizing the observables employed to probe the dynamics of the heterostructure before (gray) and after (red) excitation. e) Momentum–energy cut for the bare WSe$_2$ surface, acquired at +20 fs delay. The intensity above the white horizontal line ($E - E_F = +300$ meV) has been multiplied by 2. Both K and Σ valleys are populated. The insets show EDCs evolution within the dashed regions. f) Same as (e), but for the Au/WSe$_2$ heterostructure, at +20 fs. The intensity above the white horizontal line ($E - E_F = +300$ meV) has been multiplied by 20.

The recovery dynamics in Figure 3b reveal the mechanisms immediately subsequent the charge-transfer process: an interfacial electrical field is generated, and the increase of the Schottky barrier combines with hot-carrier relaxation to stop the hot-carrier injection. The injected carriers, after losing energy to the lattice of WSe$_2$, are rapidly back-injected to reach charge compensation, on a timescale of 250–300 fs. The charges re-injected in Au lose energy, producing the slow rise in electronic temperature observed in Figure 3a. A clear indication of the back-transfer process can be seen in Figure 3c, where the population dynamics of the Σ valley is displayed for the three cases of the bare WSe$_2$, and the heterostructure under resonant exitation and in the small detuning regime. The decay of the population

becomes strikingly faster in the heterostructure with small detuning as back-injection offers a rapid channel for charge compensation. We find the decay time of the back-injected population to be 240 ± 30 fs by constrained multiexponential fitting (see Section S7, Supporting Information).

In Figure 3c, the presence of a slow-decaying exciton population is evident at longer delays for the heterostructure. Its relative fraction changes from 72 ± 2 % to 36 ± 8 % when the excitation falls out of resonance with the A-exciton. This is the population of charge-neutral, thermalized excitons. They are formed by direct excitation with resonant pumping, and by plasmon-enhanced multiphoton absorption when the excitation is non-resonant. To support this interpretation, we measured
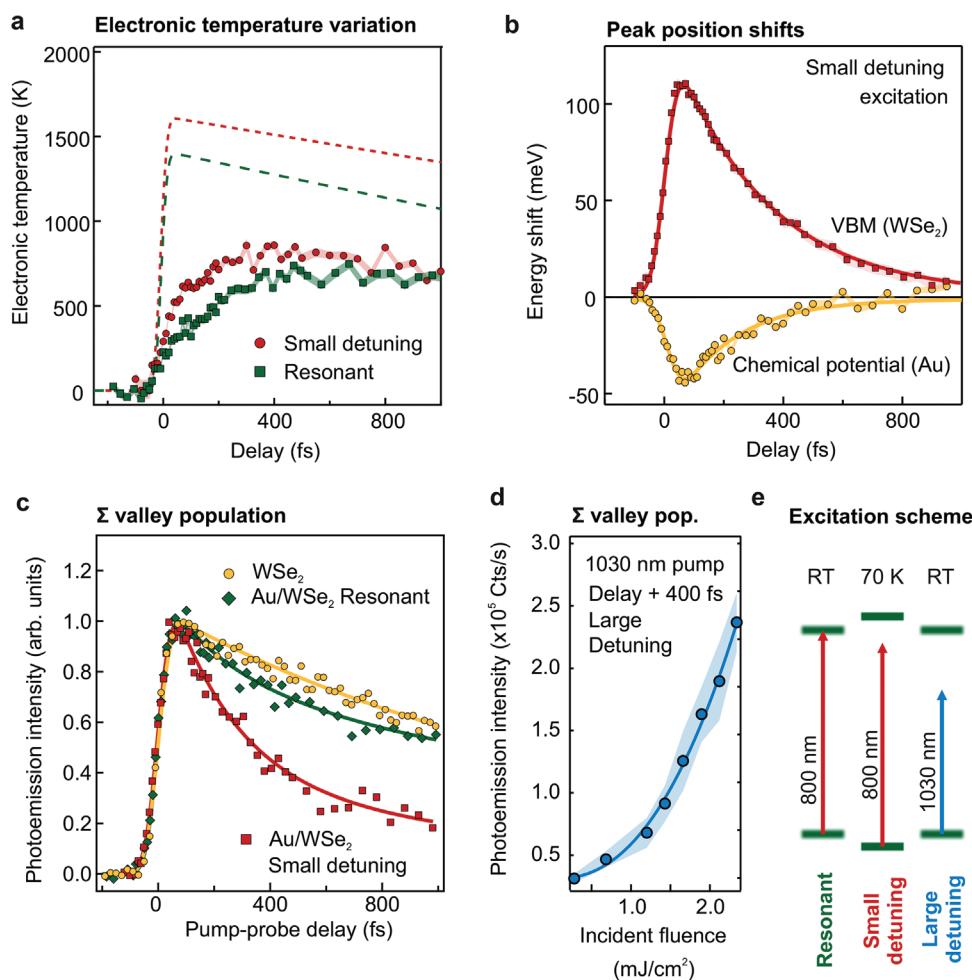
**ADVANCED
SCIENCE NEWS**

www.advancedsciencenews.com

**ADVANCED
MATERIALS**

www.advmat.de

Figure 3. Multi-observable electronic dynamics in Au/WSe$_2$. a) Electronic temperature as extracted from Fermi function fitting of the data, compared with 2TM prediction (dashed lines), using the experimental absorbed energy (from Figure 1e) and temperature-dependent experimental values of electron–phonon coupling constant, electronic and lattice heat capacities for nanostructured Au. b) Dynamic shifting of Au Fermi edge (circles) and WSe$_2$ VBM (squares). Solid lines are fits of an exponential convolved with the instrument response function (IRF). The exponential decay characteristic times are 251 ± 24 fs (Au) and 318 ± 7 fs (WSe$_2$) respectively. c) Population dynamics in the Σ valley for different experimental settings. For bare WSe$_2$, the solid line is an exponential fit convolved with the IRF, giving a decay time of 1.5 ± 0.08 ps. For the heterostructure, the solid lines are fits with double exponential decay convolved with the IRF. The second exponential is fixed at 1.5 ps, while the first is 240 ± 30 fs in both cases. The relative amplitude of the first decay changes from 36 ± 8 % to 72 ± 2 % when going from 300 to 70 K. d) Fluence dependence of the Σ valley population at long delays vs fluence for 1030 nm photoexcitation. The solid line is a power law fit resulting in an exponent of 2.3 ± 0.3. Shaded areas show the experimental uncertainty discussed in the Supporting Information. e) Schematic showing the excitation schemes employed. At room temperature, $\lambda = 800$ nm is quasi-resonant with the first excitonic transition. At 70 K, the same wavelength is slightly out of resonance, in the small detunig regime. At room temperature, $\lambda = 1030$ nm is strongly detuned, highlighting plasmonic nonlinear effects.

the fluence dependence of the Σ-valley population at long (+400 fs) pump–probe delays in the strong detuning regime (1030 nm pumping at room temperature), reported in Figure 3d (blue circles). As demonstrated by the finite element calculations (see Section S2, Supporting Information) and as expected from standard nonlinear optics consideration, long wavelengths and high fluences maximize multiphoton absorption in WSe$_2$. Figure 3e reports all the excitation schemes employed in the experiment. The population scales with fluence following a power law of exponent 2.3 ± 0.3, indicating a two-photon absorption process (see Section S7, Supporting Information). The thermalized excitons give rise to a long-timescale dynamics as they diffuse towards the nanoparticles and recombine by transferring carriers to Au, discussed in the following.

2.2. Lattice Dynamics

The vibrational response of the heterostructure is probed by FED.[31] Following optical excitation of the electrons, electron–phonon coupling increases the vibrational energy content, leading to the main quantity extracted with FED: the change of the atomic mean-squared-displacement (MSD) $\Delta\langle u^2 \rangle$.

Figure 4a shows the $\Delta\langle u^2 \rangle$ of WSe$_2$ in the first 5 ps after photoexcitation for three sets of experiments: pure WSe$_2$ pumped in resonance with the A-exciton ($\lambda = 763$ nm), Au-decorated WSe$_2$ ($\lambda = 763$ nm), and Au-decorated WSe$_2$ with sub-bandgap ($\lambda = 850$ nm) excitation—all with similar excitation density (see Experimental Section). The time-constants for lattice heating in response to resonant excitation drops from 1.73 ± 0.16 ps in
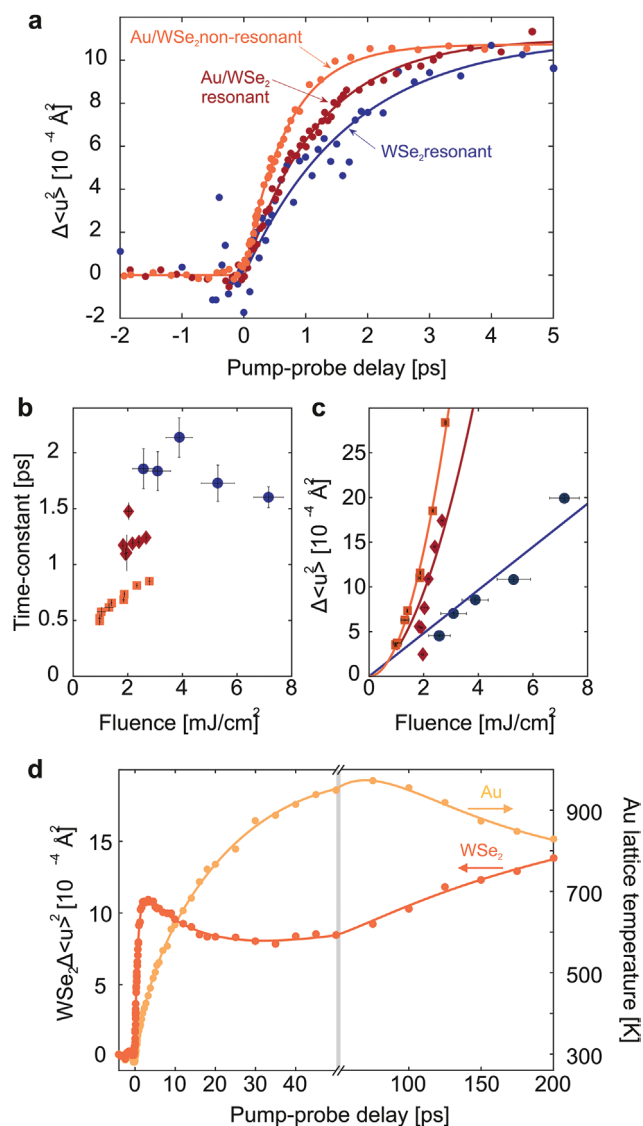
**ADVANCED
SCIENCE NEWS**

www.advancedsciencenews.com

**ADVANCED
MATERIALS**

www.advmat.de

Figure 4. Ultrafast lattice dynamics of Au/WSe$_2$ heterostructures. a) Enhancement of atomic MSD due to carrier–lattice coupling as a function of the pump–probe delay for resonant excitation of pure WSe$_2$, resonant excitation of Au/WSe$_2$, and non-resonant excitation of Au/WSe$_2$ shown with blue, red, and orange points, respectively. The corresponding solid lines are fits with exponential decay functions of the form: $Ae^{-t/\tau}$, where τ is the time-constant and A is the maximum atomic MSD caused by carrier–lattice relaxation. b,c) Time-constant for carrier–lattice coupling and maximum MSD after carrier–lattice equilibration, respectively (same color codes). d) Long delay dynamics of the atomic MSD of WSe$_2$ (orange curve and left axis) and the corresponding lattice temperature evolution of Au (gold curve and right axis).

pure WSe$_2$, to 1.19 ± 0.3 ps in Au-decorated WSe$_2$, and down to 0.68 ± 0.02 ps for sub-bandgap excitation. Pure WSe$_2$ does not show measurable lattice heating with 850 nm pumping (see Section S14, Supporting Information). From the measurements of Figure 4a, it becomes obvious that Au-decoration accelerates carrier–lattice equilibration in WSe$_2$ and enables absorption of sub-bandgap photons, giving rise to even faster lattice dynamics.

The measurements associated with the data presented in Figure 4a have been repeated for various fluences. The

extracted time-constants (τ) and amplitudes of the fitted exponential decays are plotted as a function of the incident laser fluence in Figure 4b,c respectively. Pure WSe$_2$ has a time-constant of ≈ 1.6 ps at 7 mJ cm^{-2} to ≈ 2 ps at 3 mJ cm^{-2} (Figure 4b, blue data points). With Au decoration, the WSe$_2$ lattice response to the A-exciton becomes significantly faster and all measured time-constants cluster ≈ 1.2 ps within the probed fluence range (Figure 4b, red data points). This is in clear agreement with the results of tr-ARPES experiments in Figure 3c. The accelerated lattice dynamics of WSe$_2$ results from charge-injection from Au, as the hot carriers reside only for short time in the semiconductor (Figure 3b). For pure WSe$_2$ pumped at the A-exciton resonance, the fluence dependence of the maximum MSD reached by carrier–lattice equilibration is close to linear (blue solid line, Figure 4c). When WSe$_2$ is covered by Au, the rise of the MSD is enhanced and it assumes a non-linear fluence dependence (Figure 4c).

Further acceleration of carrier–lattice relaxation is observed for sub-bandgap (850 nm) excitation (Figure 4b, orange data points). The time-constants are on the sub-picosecond timescale and as short as 500 fs at 1 mJ cm^{-2}. The non-linear fluence dependence of the maximum MSD can be represented with a power law of exponent 2.0 ± 0.1. Thus, at the high fluences used in FED, which are all higher compared to the $\lambda = 800$ nm tr-ARPES experiment, absorption of sub-bandgap photons is dominated by two-photon absorption, in line with the observations in ARPES for the Σ valley population in Figure 3d.

Figure 4d shows the lattice dynamics of Au and WSe$_2$ up to 200 ps after photoexcitation with sub-bandgap light. The MSD of Au is used to extract its lattice temperature evolution through the Debye–Waller factor. Both materials show a lattice response that can be approximated with multiexponential fitting. Regarding WSe$_2$, the MSD is first rising due to carrier–lattice relaxation with $\tau_1 = 0.74 \pm 0.02$ ps, followed by a decrease with $\tau_2 = 16 \pm 1$ ps, which we assign to phonon–phonon equilibration in WSe$_2$.[33]

In the 50–200 ps time interval, the atomic MSD of WSe$_2$ is again rising (by 5×10^{-4} Å^2, Figure 4d). The lattice dynamics of Au during the first 50 ps have bi-exponential behavior with $\tau_1 = 4 \pm 1$ ps, and $\tau_2 = 35 \pm 5$ ps. The fast, lattice-heating process is in the typical timescale (3–6 ps) for electron–phonon coupling in nano-Au, while the second is surprisingly slow for intrinsic carrier–lattice equilibration.[48,49] The slow heating can arise from the transfer of lattice-equilibrated dark excitons[27] from WSe$_2$ toward Au and their dissociation to metallic sp-states.[17] Each of these events releases ≈ 1.5 eV (the indirect bandgap of WSe$_2$) and generates hundreds of vibrational quanta. The maximum lattice temperature of Au is ≈ 970 K, while in the 50–200 ps time-interval it cools by 140 K (Figure 4d). The cooling of Au and the heating of WSe$_2$ at long time-delays is interpreted as re-equilibration of the two components by vibrational coupling, previously found in heterostructures of Au nanoclusters on various substrates.[48,49]

3. Discussion

Considering all experimental results, we can confirm the presence of a strong exciton–plasmon interaction, determine its
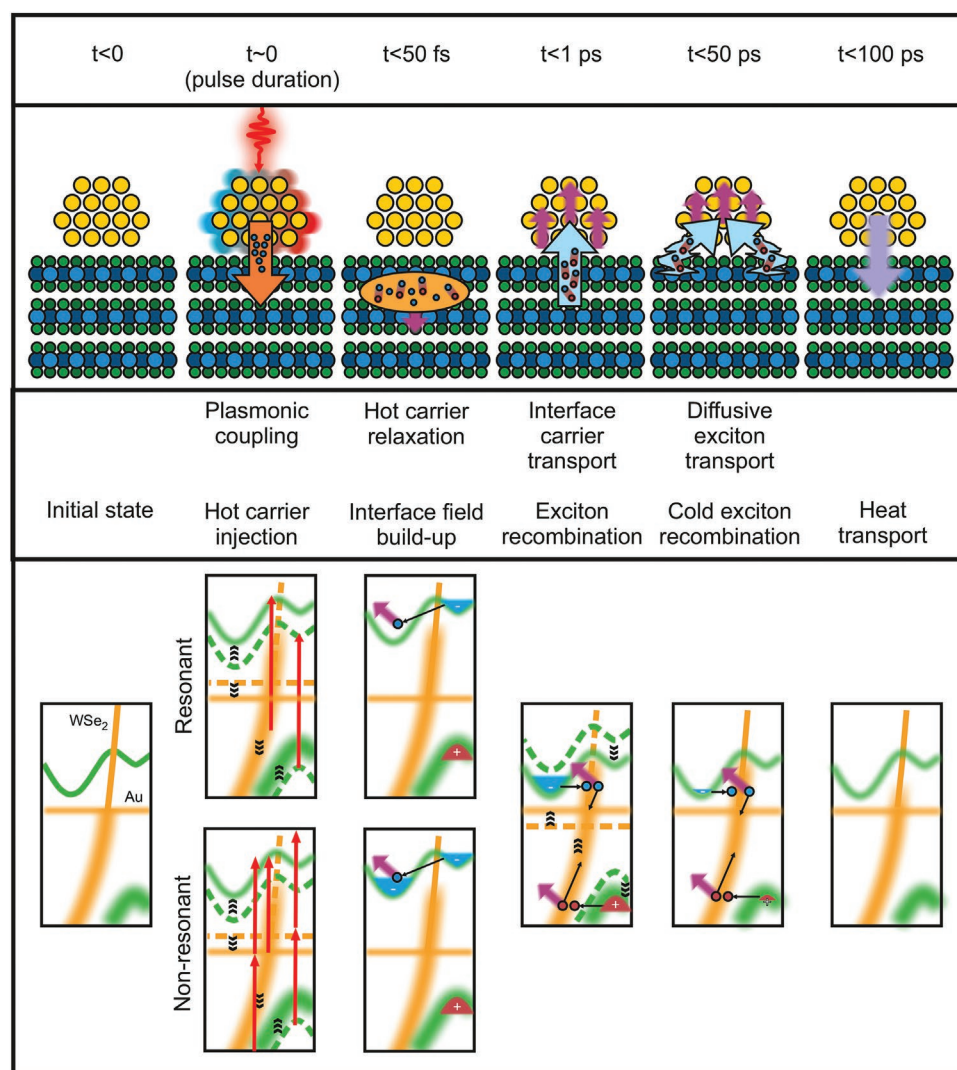
Figure 5. Energy flow across the Au/WSe$_2$ heterostructure. Schematic sequence of events and quasiparticle transfer unfolding in Au/WSe$_2$ heterostructure after near-infrared excitation. The top band shows a cartoon, real space picture. The solid orange arrows represent plasmon-induced hot-carrier transfer. The solid light-blue arrows indicate hot-exciton transfer. The wiggly light blue arrows represent diffusive exciton recombination via metallic Au states. The fuzzy purple arrows indicate hot-phonon generation by electron–phonon coupling. The fuzzy lilac arrow shows the direction of vibrational energy transfer at long timescales. The bottom panel shows the correspnding electronic structure picture, with the two different cases of resonant and sub-bandgap pumping separated at short timescales. The red arrows indicate the relevant vertical optical transitions.

microscopic origin, and assess the kinematics of the multi-directional energy flow across the interface. **Figure 5** summarizes the observed processes in the Au/WSe$_2$ heterostructure in real-space (upper panels) and momentum-space (lower panels). In the interpretation of the data, it is important to notice that, while FED probes the entire volume of the sample, tr-ARPES is extremely surface sensitive: for this reason we focus on observables that are homogeneous at the scale of a nanoparticle or a gap (≈10 nm) at the timescales of interest (>10 fs), or we use the excitation wavelength to be intrinsically selective of the hot carriers while tracking population dynamics (see Section S10, Supporting Information).

Optical illumination induces LSP at the nanoisland's surfaces and edges. In Au, plasmons produce highly energetic hot carriers that scatter across the interface on extremely short

timescales (<10s fs). Both electrons and holes are transferred, but the asymmetric Schottky barrier produces an excess electron population. In the WSe$_2$ gaps not covered by Au, the strong near-fields generate electrons and holes through non-linear multiphoton absorption: this gains relevance over hot-carrier injection or single-photon absorption at wavelengths ≥850 nm and fluences ≥1 mJ cm^{-2}.

After excitation, most of the injected hot carriers lose their energy in WSe$_2$ forming indirect (optically dark) excitons. Initially, when the carriers enter the semiconductor ballistically, they may undergo electronic scattering processes such as electron–electron, electron–hole and surface/defect scattering to relax to a thermalized hot carrier distribution. Subsequently, the hot carriers transfer energy to the lattice predominantly via electron–phonon scattering, with possible contributions of

**ADVANCED
SCIENCE NEWS**

www.advancedsciencenews.com

**ADVANCED
MATERIALS**

www.advmat.de

surface/defect-assisted collisions. Singling out the individual contributions of each mechanism is beyond the scope of this work, and would require targeted experiments. We will therefore refer to these transitional phases with the general terms "hot carrier relaxation" and "electron–phonon relaxation."

Then, the hot unbalanced free electrons, confined by static and dynamic interfacial fields to the vicinity (<1 nm) of the nanoisland, flow back to Au, re-equilibrating charge on a timescale of 240 ± 30 fs. The electronic temperature of Au raises only through carrier backflow on hundreds of femtoseconds timescales, in stark contrast with the classic model of plasmonics assuming thermalization of the metallic hot carriers before interfacial transfer.

In parallel, the hot carriers generated by non-linear multiphoton absorption, distributed in the crystal, turn into dark excitons by electron–phonon coupling with the lattice at sub-picosecond timescales due to their large scattering phase-space. Both of these processes shorten the electron–lattice relaxation time of WSe_2 down to 500 fs for low fluence (≤1 mJ cm^{-2}) and sub-bandgap (≥850 nm) pumping. After electron–lattice relaxation in WSe_2 (t > 1 ps), the remaining cold dark excitons move diffusively until they reach the nanoislands, where they dissociate and produce a second intense lattice-heating of Au on a timescale of 35 ± 5 ps. This process is maximized when using sub-bandgap pumping at high fluences, where nonlinear multiphoton effects generate large populations of dark excitons in the plasmonic hotspots appearing in a few tens of nanometers radius from the interface.

4. Conclusion

We have disentangled the contributions of individual materials and specific plasmonic, electronic and phononic excitations to interfacial energy transfer processes. We have demonstrated that strong plasmon–exciton interaction leads to immediate energy transfer to the semiconductor, with the nanometal being heated by carrier backflow and exciton recombination at two distinct timescales. The two-stepped energy backflow arises from the presence of two species of excitons: the ones generated by strong plasmon–exciton interaction in the vicinity of the nanoisland and the ones produced by non-linear absorption in the plasmonic hot-spots.

The Au/WSe_2 system is close to real-life applications, with the Au nanoislands offering plasmonic and catalytic properties and the WSe_2 displaying a rich excitonic structure that allows following different energy paths at different photon energies. The possibility of harvesting plasmonic energy into high energy excitons is a mechanism useful for optoelectronics and photochemistry,[39] and the backflow arising from recombination might be minimized by careful engineering of the band alignment and momentum-matching conditions. The subsequent energy flow causing intense, local, lattice heating of nanoscale Au is a quasi-thermal process that can be used for photothermal conversion and for catalyzing chemical reactions.[50] These findings offer new possibilities to tune the quasi-thermal response by controlling the exciton population, possibly with means other than multi-wavelength and fluence excitation protocol employed here. For example, interfacing Au nanoislands with more complex 2D semiconducting heterostructures[51] might allow electrical control of the exciton population and thus of photochemical performance. Even further, manipulating the valley degree of freedom might give access to band topology-controlled functionalities.[20,23]

5. Experimental Section

Time-Resolved ARPES: The time-resolved ARPES experiments were performed using a home-built optical parametric chirped-pulse amplifier (OPCPA) with 500 kHz repetition rate.[52] The OPCPA is used to drive high-order harmonic generation (HHG) by tightly focusing laser pulses onto an argon gas jet. The HHG produces a comb of odd harmonics of the driving laser, extending up to the 11th order. The co-propagating fundamental is separated from the XUV harmonic beam using reflection onto a silicon wafer at Brewster's angle. A single harmonic (7th order, 21.7 eV, p-polarized, pulse duration: 23 ± 4 fs FWHM, energy width: 110 meV FWHM) is isolated by reflection off a focusing multilayer XUV mirror and transmission through a 400 nm-thick Sn metallic filter. A photon flux of up to 2 × 10^{11} photons s^{-1} at the sample position is achieved.[53] The 800 nm pump was s-polarized, had pulse duration of 36 ± 4 fs, incident fluence of 750 ± 50 μJ. The 1030 nm pump was s-polarized, had pulse duration of approx. 250 fs, and variable incident fluence. The bulk WSe_2 samples were handled by a 6-axis manipulator (SPECS GmbH). The data were acquired using a time-of-flight momentum microscope (METIS1000, SPECS GmbH) and processed using custom-built code[54] for Figure 2c, while all the dynamics was measured using a hemispherical electron spectrometer (PHOIBOS150, SPECS GmbH) to achieve higher statistical performance.[55]

Femtosecond Electron Diffraction: The FED apparatus employed electron pulses to measure the ultrafast lattice dynamics in response to photoexcitation. The diameters of the probed and pumped (photoexcited) areas were 100 and 400 μm, respectively. For each diffraction peak, the intensity was extracted by direct integration of the total counts within a circle of 20 pixel diameter. The center of the circle coincided with the center of mass of the peak, and it was recalculated for each diffraction pattern in order to eliminate the effect of instabilities of the electron gun and the magnetic lens. An ultrashort laser pulse (100 fs) of selected wavelength (TOPAS Prime NirUVis) excited the electronic subsystem. The lattice response was probed with a time-resolution in the order of 300 fs using ultrashort, high energy (60 keV) electrons pulses[31] that impinged on the thin, freestanding sample, producing a diffraction pattern in transmission (Figure S9a, Supporting Information). After the arrival of an ultrashort laser pulse, the intensity of all diffraction peaks (I_{hkl}) decreased, and the inelastic scattering background increased, due to the generation of phonons by excited charge carriers and the Debye–Waller effect.

The relative decay of the diffraction peaks was used to calculate the time-dependent change of the atomic MSD ($\Delta\langle u^2 \rangle$) through the formula:

$$\Delta\langle u^2 \rangle = -\frac{3d_{hkl}^2}{4\pi^2}\ln\frac{I_{hkl}(t)}{I_{hkl}(t<0)} \tag{1}$$

where d_{hkl} is the spacing between crystal planes for each diffraction peak. For each measurement the $\Delta\langle u^2 \rangle$ is averaged over all the diffraction peaks. Thus, the present analysis does not explicitly take into account nonthermal lattice modes[56] and the distinct vibrational amplitudes for different types of atoms in compounds, since the aim is to compare the average MSD dynamics[33] for pure and Au-decorated WSe_2. For this purpose, the measurements of Figure 4a have been performed adjusting the fluence in order to obtain the same maximum atomic MSD of (10.99 ± 0.09) × 10^{-4} Å^2. For pure WSe_2, the incident laser fluence was (5.3 ± 0.6) mJ cm^{-2}, while for Au-decorated WSe_2, it was (2.18 ± 0.04) mJ cm^{-2} for A-exciton pumping and (1.88 ± 0.02) mJ cm^{-2} for sub-bandgap photoexcitation.

Sample Preparation: Samples for ARPES were prepared by cleaving bulk WSe_2 crystals in vacuum (base pressure better than 5 × 10^{-11} mbar).

The crystals were then cooled to 70 K, then Au was evaporated on the surface for 5 min at a calibrated rate of 2 ± 1 Å min^{-1}. The deposition at low temperature ensures homogeneous coverage across the sample. The sample was then "annealed" at 300 K for 30 min to enable island formation before measurement. The average height of the nanoislands was calculated at 2 ± 1 nm by considering nominal film thickness (1 ± 0.5 nm) and average area coverage ($\approx 50\%$).

The multilayer free-standing membranes for the FED measurements were prepared by exfoliation from bulk single crystals (HQ Graphene). Large flakes of WSe_2 were first separated from the bulk single crystal with a lancet. Then the flakes were attached on a glass substrate with a water soluble glue (Crystalbond) and thinned down by exfoliation with a scotch tape. The thin areas of WSe_2 were then separated from the substrate with a scalpel and placed into water to separate WSe_2 from the glue. Finally, the floating flakes of WSe_2 were scooped out with a TEM copper grid held by a tweezer and left to dry. For the Au/WSe_2, the TEM copper grid with the flake was placed in a UHV chamber, and 2 nm of Au were evaporated on top with electron-beam-evaporation using a rotating sample holder for homogeneous deposition.

Optical Measurements: Using optical microscopy, a spot was selected on a thin flake of bare WSe_2 (≈ 20 nm) suspended over a TEM grid, choosing a flat (without wrinkles) part of the sample. For this point of the sample, the optical transmission and reflectance spectra (T and R, respectively) were recorded using a micro-absorbance spectrometer, a supercontinuum laser (FIANIUM) as the broadband light source, and a fiber spectrometer (Avantes). In all cases, dark and reference spectra were recorded. The absorption spectrum (A in %) was calculated as A=100-T-R. Subsequently, the flake was decorated with 2 nm-thick Au, and the measurements were repeated at the same spot on the sample.

Finite Element Calculations: To understand the distribution of fields at the surface and explore the linear response of the heterostructure, the optical response was simulated in the frequency domain using the Optics package in the commercial finite difference software COMSOL Multiphysics. A block of 100 nm × 200 nm × 500 nm was used to model the substrate, while 2 nm-thick islands were extruded on the surface using a lateral profile extracted from a micrograph, to exactly match the effective spatial distribution. A 100 nm × 200 nm × 500 nm vacuum layer was added on top. The optical field was incident vertically with polarization along the x direction (maps in Figure 1 are rotated 90°). The mesh was optimized to achieve minimum element quality (skeweness) >0.1. The cuboid was surrounded by periodic boundary conditions, except for the input and output planes (along the z-direction), where perfectly matched layer conditions were used.

To evaluate the LSP-generated hot carrier photocurrent, the following expression was integrated:

$$P = \int_{V_{Au}} |E|^2 \, dr \tag{2}$$

over the nanoparticle volume. As discussed in Ref. [38], this is proportional to the number of LSP-generated hot-carriers crossing the interface in a Schottky junction. To calculate the local the field enhancement $|E|/|E_0|$, the ratio between $|E|$, the modulus of the electric field in the heterostructure, and $|E_0|$ the modulus of the electrical field in absence of Au were simply evaluated.

The presence of both hot-carrier dominated photoabsorption and field enhancement was robust against variations in the shape and thickness of the islands, including islands with Winterbottom shape that represented the equilibrium configuration at high temperatures,[57] as long as the average coverage of 50% with typical sizes of islands and gaps ≈ 10 nm were preserved.

Statistical Analysis: Time-of-flight generated multidimensional ARPES data were preprocessed by binning the tabular data structure into 4D hypervolumetric data. During the binning procedure, image distortion correction, image registration, momentum, energy, and pump–probe delay calibrations were applied according to the procedure described elsewhere.[54] Hemispherical analyzer ARPES data do not require binning.

Calibration-based distortion correction, together with momentum, energy and pump–probe delay calibration were applied in the preprocessing phase. The pump–probe time-traces were averaged over multiple scans of the delay stage. Data are presented using mean ± standard deviation (SD), i.e. 68% confidence intervals. The fitting procedures employed are based on the non-linear least square method. Data analysis is performed using custom built routines in the proprietary software IgorPro.

The raw diffraction patterns were corrected by dark image subtraction (electron beam off and same exposure time) and flat field correction (obtained with homogeneous illumination of the electron camera with a strongly defocused polycrystalline diffraction pattern). The intensity of each Bragg spot was integrated over a circular area, whose center matched the position of local maximum intensity. The pump–probe time-traces were averaged over multiple scans of the delay stage. The time-constants and amplitudes, extracted by nonlinear least squares fitting of exponential decay functions, have error bars representing the 68% confidence intervals. Data analysis was performed with custom built Matlab scripts.

Supporting Information

Supporting Information is available from the Wiley Online Library or from the author.

Acknowledgements

Conflict of Interest

The authors declare no conflict of interest.

Data Availability Statement

We provide the full experimental dataset as well as the details of the data analysis on the data repository Zenodo (https://doi.org/10.5281/zenodo.7441232). The source code for the tr-ARPES data analysis is available on GitHub (https://github.com/mpes-kit).

Keywords

[1] M. Moskovits, *Nat. Nanotechnol.* **2015**, *10*, 6.

[2] M. L. Brongersma, N. J. Halas, P. Nordlander, *Nat. Nanotechnol.* **2015**, *10*, 25.

[3] S. Linic, S. Chavez, R. Elias, *Nat. Mater.* **2021**, *20*, 916.

[4] H. A. Atwater, A. Polman, *Nat. Mater.* **2010**, *9*, 205.

[5] C. Clavero, *Nat. Photonics* **2014**, *8*, 95.

[6] A. Furube, S. Hashimoto, *NPG Asia Mater.* **2017**, *9*, e454.

[7] J. Langer, D. Jimenez de Aberasturi, J. Aizpurua, R. A. Alvarez-Puebla, B. Auguié, J. J. Baumberg, G. C. Bazan, S. E. J. Bell, A. Boisen, A. G. Brolo, J. Choo, D. Cialla-May, V. Deckert, L. Fabris, K. Faulds, F. J. García de Abajo, R. Goodacre, D. Graham, A. J. Haes, C. L. Haynes, C. Huck, T. Itoh, M. Käll, J. Kneipp, N. A. Kotov, H. Kuang, E. C. Le Ru, H. K. Lee, J.-F. Li, X. Y. Ling, et al., *ACS Nano* **2020**, *14*, 28.

[8] P. K. Jain, K. S. Lee, I. H. El-Sayed, M. A. El-Sayed, *J. Phys. Chem. B* **2006**, *110*, 7238.

[9] J. B. Khurgin, *Nat. Nanotechnol.* **2015**, *10*, 2.

[10] C. Boerigter, R. Campana, M. Morabito, S. Linic, *Nat. Commun.* **2016**, *7*, 10545.

[11] G. V. Hartland, L. V. Besteiro, P. Johns, A. O. Govorov, *ACS Energy Lett.* **2017**, *2*, 1641.

[12] S. Tan, A. Argondizzo, J. Ren, L. Liu, J. Zhao, H. Petek, *Nat. Photonics* **2017**, *11*, 806.

[13] G. Tagliabue, J. S. DuChene, M. Abdellah, A. Habib, D. J. Gosztola, Y. Hattori, W.-H. Cheng, K. Zheng, S. E. Canton, R. Sundararaman, J. Sá, H. A. Atwater, *Nat. Mater.* **2020**, *19*, 1312.

[14] A. M. Brown, R. Sundararaman, P. Narang, A. M. Schwartzberg, W. A. Goddard III, H. A. Atwater, *Phys. Rev. Lett.* **2017**, *118*, 087401.

[15] M.-E. Kleemann, R. Chikkaraddy, E. M. Alexeev, D. Kos, C. Carnegie, W. Deacon, A. C. De Pury, C. Große, B. De Nijs, J. Mertens, A. I Tartakovskii, J. J Baumberg, *Nat. Commun.* **2017**, *8*, 1296.

[16] X. Yan, H. Wei, *Nanoscale* **2020**, *12*, 9708.

[17] A. Grubišić Čabo, J. A. Miwa, S. S. Grønborg, J. M. Riley, J. C. Johannsen, C. Cacho, O. Alexander, R. T. Chapman, E. Springate, M. Grioni, J. V. Lauritsen, P. D. C. King, P. Hofmann, S. Ulstrup, *Nano Lett.* **2015**, *15*, 5883.

[18] J. Vogelsang, L. Wittenbecher, D. Pan, J. Sun, S. Mikaelsson, C. L. Arnold, A. L'Huillier, H. Xu, A. Mikkelsen, *ACS Photonics* **2021**, *8*, 1607.

[19] C. Xu, H. W. Yong, J. He, R. Long, A. R. Cadore, I. Paradisanos, A. K. Ott, G. Soavi, S. Tongay, G. Cerullo, A. C. Ferrari, O. V. Prezhdo, Z.-H. Loh, *ACS Nano* **2020**, *15*, 819.

[20] L. Li, L. Shao, X. Liu, A. Gao, H. Wang, B. Zheng, G. Hou, K. Shehzad, L. Yu, F. Miao, Y. Shi, Y. Xu, X. Wang, *Nat. Nanotechnol.* **2020**, *15*, 743.

[21] H. Shan, Y. Yu, X. Wang, Y. Luo, S. Zu, B. Du, T. Han, B. Li, Y. Li, J. Wu, F. Lin, K. Shi, B. K. Tay, Z. Liu, X. Zhu, Z. Fang, *Light: Sci. Appl.* **2019**, *8*, 9.

[22] J. R. Dunklin, A. H. Rose, H. Zhang, E. M. Miller, J. van de Lagemaat, *ACS Photonics* **2020**, *7*, 197.

[23] W.-H. Lin, P. C. Wu, H. Akbari, G. R. Rossman, N.-C. Yeh, H. A. Atwater, *Adv. Mater.* **2022**, *34*, 2104863.

[24] M. Dendzik, A. Bruix, M. Michiardi, A. S. Ngankeu, M. Bianchi, J. A. Miwa, B. Hammer, P. Hofmann, C. E. Sanders, *Phys. Rev. B* **2017**, *96*, 235440.

[25] N. F. Hinsche, A. S. Ngankeu, K. Guilloy, S. K. Mahatha, A. G. Čabo, M. Bianchi, M. Dendzik, C. E. Sanders, J. A. Miwa, H. Bana, E. Travaglia, P. Lacovig, L. Bignardi, R. Larciprete, A. Baraldi, S. Lizzit, K. S. Thygesen, P. Hofmann, *Phys. Rev. B* **2017**, *96*, 121402.

[26] A. Varas, P. García-González, J. Feist, F. García-Vidal, A. Rubio, *Nanophotonics* **2016**, *5*, 409.

[27] R. Bertoni, C. W. Nicholson, L. Waldecker, H. Hübener, C. Monney, U. De Giovannini, M. Puppin, M. Hoesch, E. Springate, R. T. Chapman, C. Cacho, M. Wolf, A. Rubio, R. Ernstorfer, *Phys. Rev. Lett.* **2016**, *117*, 277201.

[28] C. W. Nicholson, A. Lücke, W. G. Schmidt, M. Puppin, L. Rettig, R. Ernstorfer, M. Wolf, *Science* **2018**, *362*, 821.

[29] S. Dong, M. Puppin, T. Pincelli, S. Beaulieu, D. Christiansen, H. Hübener, C. W. Nicholson, R. P. Xian, M. Dendzik, Y. Deng, Y. W. Windsor, M. Selig, E. Malic, A. Rubio, A. Knorr, M. Wolf, L. Rettig, R. Ernstorfer, *Nat. Sci.* **2021**, *1*, e10010.

[30] M. Sygletou, S. Benedetti, M. Ferrera, G. M. Pierantozzi, R. Cucini, G. Della Valle, P. Carrara, A. De Vita, A. di Bona, P. Torelli, D. Catone, G. Panaccione, M. Canepa, F. Bisio, *Small* **2021**, *17*, 2100050.

[31] L. Waldecker, R. Bertoni, R. Ernstorfer, *J. Appl. Phys.* **2015**, *117*, 044903.

[32] L. Waldecker, T. A. Miller, M. Rudé, R. Bertoni, J. Osmond, V. Pruneri, R. E. Simpson, R. Ernstorfer, S. Wall, *Nat. Mater.* **2015**, *14*, 991.

[33] L. Waldecker, R. Bertoni, H. Hübener, T. Brumme, T. Vasileiadis, D. Zahn, A. Rubio, R. Ernstorfer, *Phys. Rev. Lett.* **2017**, *119*, 036803.

[34] G. Nicolay, R. Claessen, F. Reinert, V. Strocov, S. Hüfner, H. Gao, U. Hartmann, E. Bucher, *Surf. Sci.* **1999**, *432*, 95.

[35] A. C. Domask, K. A. Cooley, B. Kabius, M. Abraham, S. E. Mohney, *Cryst. Growth Des.* **2018**, *18*, 3494.

[36] K. A. Cooley, R. Alsaadi, R. L. Gurunathan, A. C. Domask, L. Kerstetter, W. A. Saidi, S. E. Mohney, *J. Cryst. Growth* **2019**, *505*, 44.

[37] H. Sun, M. Yu, G. Wang, X. Sun, J. Lian, *J. Phys. Chem. C* **2012**, *116*, 9000.

[38] B. Y. Zheng, H. Zhao, A. Manjavacas, M. McClain, P. Nordlander, N. J. Halas, *Nat. Commun.* **2015**, *6*, 7797.

[39] A. Manjavacas, J. G. Liu, V. Kulkarni, P. Nordlander, *ACS Nano* **2014**, *8*, 7630.

[40] A. O. Govorov, H. Zhang, Y. K. Gun'ko, *J. Phys. Chem. C* **2013**, *117*, 16616.

[41] A. M. Brown, R. Sundararaman, P. Narang, W. A. Goddard III, H. A. Atwater, *ACS Nano* **2016**, *10*, 957.

[42] Y. Zhang, O. Pluchery, L. Caillard, A.-F. Lamic-Humblot, S. Casale, Y. J. Chabal, M. Salmeron, *Nano Lett.* **2015**, *15*, 51.

[43] C. M. Smyth, R. Addou, S. McDonnell, C. L. Hinkle, R. M. Wallace, *2D Mater.* **2017**, *4*, 025084.

[44] G. Wang, A. Chernikov, M. M. Glazov, T. F. Heinz, X. Marie, T. Amand, B. Urbaszek, *Rev. Mod. Phys.* **2018**, *90*, 021001.

[45] M. Selig, G. Berghäuser, M. Richter, R. Bratschitsch, A. Knorr, E. Malic, *2D Mater.* **2018**, *5*, 035017.

[46] M. Massicotte, P. Schmidt, F. Vialla, K. G. Schädler, A. Reserbat-Plantey, K. Watanabe, T. Taniguchi, K.-J. Tielrooij, F. H. Koppens, *Nat. Nanotechnol.* **2016**, *11*, 42.

[47] A. Arora, M. Koperski, K. Nogajewski, J. Marcus, C. Faugeras, M. Potemski, *Nanoscale* **2015**, *7*, 10421.

[48] T. Vasileiadis, L. Waldecker, D. Foster, A. Da Silva, D. Zahn, R. Bertoni, R. E. Palmer, R. Ernstorfer, *ACS Nano* **2018**, *12*, 7710.

[49] T. Vasileiadis, E. N. Skountzos, D. Foster, S. P. Coleman, D. Zahn, F. Krečinić, V. G. Mavrantzas, R. E. Palmer, R. Ernstorfer, *Nanoscale Horiz.* **2019**, *4*, 1164.

**ADVANCED
SCIENCE NEWS**

www.advancedsciencenews.com

**ADVANCED
MATERIALS**

www.advmat.de

[50] Y. Dubi, I. W. Un, Y. Sivan, *Chem. Sci.* **2020**, *11*, 5017.

[51] C. Jin, E. Y. Ma, O. Karni, E. C. Regan, F. Wang, T. F. Heinz, *Nat. Nanotechnol.* **2018**, *13*, 994.

[52] M. Puppin, Y. Deng, O. Prochnow, J. Ahrens, T. Binhammer, U. Morgner, M. Krenz, M. Wolf, R. Ernstorfer, *Opt. Express* **2015**, *23*, 1491.

[53] M. Puppin, Y. Deng, C. Nicholson, J. Feldl, N. Schröter, H. Vita, P. Kirchmann, C. Monney, L. Rettig, M. Wolf, R. Ernstorfer, *Rev. Sci. Instrum.* **2019**, *90*, 023104.

[54] R. P. Xian, Y. Acremann, S. Y. Agustsson, M. Dendzik, K. Bühlmann, D. Curcio, D. Kutnyakhov, F. Pressacco, M. Heber, S. Dong, T. Pincelli, J. Demsar, W. Wurth, P. Hofmann, M. Wolf, M. Scheidgen, L. Rettig, R. Ernstorfer, *Sci. Data* **2020**, *7*, 442.

[55] J. Maklar, S. Dong, S. Beaulieu, T. Pincelli, M. Dendzik, Y. W. Windsor, R. P. Xian, M. Wolf, R. Ernstorfer, L. Rettig, *Rev. Sci. Instrum.* **2020**, *91*, 123112.

[56] L. Waldecker, R. Bertoni, R. Ernstorfer, J. Vorberger, *Phys. Rev. X* **2016**, *6*, 021003.

[57] K. Reidy, J. D. Thomsen, H. Y. Lee, V. Zarubin, Y. Yu, B. Wang, T. Pham, P. Periwal, F. M. Ross, *Nano Lett.* **2022**, *22*, 5849.